frontiers | Frontiers in Electronic Materials

TYPE Original Research
PUBLISHED 07 September 2023
DOI 10.3389/femat.2023.1246016

OPEN ACCESS

EDITED BY
Pashupati Dhakal,
Jefferson Lab (DOE), United States

REVIEWED BY
Akira Miyazaki,
UMR9012 Laboratoire de Physique des 2 infinis Irène Joliot-Curie (IJCLab), France
Gianluigi Catelani,
Forschungszentrum Jülich, Germany

*CORRESPONDENCE
W. P. M. R. Pathirana,
walivepathiranagemr@vmi.edu

RECEIVED 24 June 2023
ACCEPTED 15 August 2023
PUBLISHED 07 September 2023

CITATION
Pathirana WPMR and Gurevich A (2023), Superheating field in superconductors with nanostructured surfaces.
Front. Electron. Mater. 3:1246016.
doi: 10.3389/femat.2023.1246016

Superheating field in superconductors with nanostructured surfaces

W. P. M. R. Pathirana[1]* and A. Gurevich[2]

[1]Department of Physics and Astronomy, Virginia Military Institute, Lexington, VA, United States, [2]Department of Physics and Center for Accelerator Science, Old Dominion University, Norfolk, VA, United States

We report calculations of a DC superheating field H_{sh} in superconductors with nanostructured surfaces. Numerical simulations of the Ginzburg–Landau (GL) equations were performed for a superconductor with an inhomogeneous impurity concentration, a thin superconducting layer on top of another superconductor, and superconductor–insulator–superconductor (S-I-S) multilayers. The superheating field was calculated taking into account the instability of the Meissner state with a non-zero wavelength along the surface, which is essential for the realistic values of the GL parameter κ. Simulations were performed for the material parameters of Nb and Nb_3Sn at different values of κ and the mean free paths. We show that the impurity concentration profile at the surface and thicknesses of S-I-S multilayers can be optimized to enhance H_{sh} above the bulk superheating fields of both Nb and Nb_3Sn. For example, an S-I-S structure with a 90-nm-thick Nb_3Sn layer on Nb can boost the superheating field up to ≈500 mT, while protecting the superconducting radio-frequency (SRF) cavity from dendritic thermomagnetic avalanches caused by local penetration of vortices.

KEYWORDS

superheating field, superconductors, multilayered superconductors, vortices, Ginzburg–Landau theory

1 Introduction

The superconducting radio-frequency (SRF) resonant cavities in particle accelerators enable high accelerating gradients with low power consumption. The best Nb cavities can have high quality factors $Q \sim 10^{10}$–10^{11} and sustain accelerating fields up to 50 MV/m at $T = 1.5$–2 K and 0.6–2 GHz (Padamsee et al., 2018; Gurevich, 2023). The peak RF fields $B_0 \simeq 200$ mT at the equatorial surface of Nb cavities can approach the thermodynamic critical field $B_c \approx 200$ mT at which the screening current density flowing at the inner cavity surface is close to the depairing current density $J_c \simeq B_c/\mu_0\lambda$—the maximum DC current density a superconductor can carry in the Meissner state (Tinkham, 2004), where λ is the penetration depth of the magnetic field. Thus, the breakdown fields of the best Nb cavities have nearly reached the DC superheating field $B_{sh} \simeq B_c$ (Galaiko, 1966; Matricon and Saint-James, 1967; Christiansen, 1969; Chapman, 1995; Catelani and Sethna, 2008; Transtrum et al., 2011; Lin and Gurevich, 2012). The Q factors can be increased by material treatments such as high-temperature annealing followed by low-temperature baking which not only increase Q (B_0) and the breakdown field but also reduce the deterioration of Q at high fields (Ciovati et al., 2010; Posen et al., 2020). High-temperature treatments combined with the infusion of nitrogen, titanium,

or oxygen can produce an anomalous increase of Q (B_0) with RF field amplitude $B_0 = \mu_0 H_0$ (Ciovati et al., 2016; Grassellino et al., 2017; Dhakal, 2020; Lechner et al., 2021). These advances raise the question about the fundamental limit of the breakdown fields of SRF cavities and the extent to which it can be pushed by surface nanostructuring and impurity management (Gurevich and Kubo, 2017; Gurevich, 2023).

Several ways of increasing the SRF breakdown fields by surface nanostructuring have been proposed. They include depositing high-T_c superconducting multilayers with thin dielectric interlayers (Gurevich, 2006; Gurevich, 2015; Kubo et al., 2014; Liarte et al., 2017; Kubo, 2021) or a dirty overlayer with a higher impurity concentration at the surface (Ngampruetikorn and Sauls, 2019). The DC superheating field of such structures has been evaluated using the London, Ginzburg–Landau (GL), and quasiclassical Usadel and Eilenberger equations in the limit of an infinite GL parameter $\kappa = \lambda/\xi \to \infty$ in which the breakdown of the Meissner state at $H_0 = H_{sh}$ occurs once the current density at the surface reaches the depairing limit (Gurevich, 2006; Gurevich, 2015; Kubo et al., 2014; Liarte et al., 2017; Kubo, 2021; Ngampruetikorn and Sauls, 2019). Yet, it has been well-established that in a more realistic case of a finite κ, the breakdown of the Meissner state at $H = H_{sh}$ occurs due to the exponential growth of periodic perturbations of the order parameter and the magnetic field with a wavelength $\lambda_c \sim (\xi^3\lambda)^{1/4}$ along the surface, where ξ is the coherence length (Christiansen, 1969; Chapman, 1995; Transtrum et al., 2011). The effect of such periodic Turing instability (Cross and Hohenberg, 1993) on H_{sh} can be particularly important for Nb cavities with $\kappa \sim 1$. Addressing the effect of finite κ (which in turn depends on the mean free path) on H_{sh} in superconductors with nanostructured surfaces is the goal of this work.

We present the results of numerical calculations of a DC superheating field for different superconducting geometries in materials with finite κ and determine optimal surface nanostructures that can withstand the maximum magnetic field in the vortex-free Meissner state. In particular, we consider a bulk superconductor with a thin impurity diffusion layer, a clean superconducting overlayer separated by an insulating layer from the bulk (e.g., Nb_3Sn-I-Nb_3Sn), a thin dirty superconducting layer on the top of the same superconductor (e.g., dirty Nb_3Sn-I-clean Nb_3Sn), and a thin high-T_c superconducting layer on the top of a low-T_c superconductor (e.g., Nb_3Sn-I-Nb). We calculate H_{sh} and determine an optimal layer thickness for each geometry by numerically solving the GL equations, taking into account both the non-linear screening of the applied magnetic field and the periodic instability of the Meissner state in a nanostructured superconductor.

The paper is organized as follows. The GL equations and methods of numerical detection of H_{sh} and the wavelength λ_c of a critical perturbation causing the instability of the Meissner state are presented in Section 2. The results of numerical calculations of H_{sh} for impurity diffusion layers and various S-I-S structures are given in Section 3 and Section 4, respectively. Section 5 contains discussion of the results, and Section 6 provides the conclusion with a summary. Computational details are given in Section Method and other technical details are given in Supplementary Appendices A, B.

2 GL equations and numerical detection of H_{sh} and k_c

We first consider a semi-infinite uniform superconductor in a magnetic field H_0 applied along the z-axis, parallel to the planar surface. In this case, the induced supercurrents flow in the xy plane and GL equations for the complex order parameter $\psi = \Delta e^{i\varphi}$, and two components of the vector potential A_x and A_y can be reduced to two coupled partial differential equations for the amplitude $\Delta(x, y, t)$ and the z-component of the magnetic field H (x, y, t). As shown in Supplementary Appendix A, these equations can be written in the following dimensionless form:

$$\dot{f} - f + f^3 - \nabla^2 f + \frac{\kappa^2}{f^3}\left[(\partial_x h)^2 + \left(\partial_y h\right)^2\right] = 0, \tag{1}$$

$$\nabla \cdot \left(\frac{\nabla h}{f^2}\right) = \frac{h}{\kappa^2}. \tag{2}$$

Here, $f(x, y) = \Delta(x, y)/\Delta_0$, $\Delta_0(T)$ is the equilibrium order parameter in the bulk, $h(x, y) = H(x, y)/\sqrt{2}H_c$, and all lengths are in units of the coherence length ξ and $\kappa = \lambda/\xi$. Despite the presence of the time derivative $\dot{f}$ in Eqs (1, 2), they are essentially the quasi-static GL equations, but not the true time-dependent Ginzburg–Landau (TDGL) equations (Watts-Tobin et al., 1981; Sheikhzada and Gurevich, 2020) which describe a non-equilibrium superconductor at $T \approx T_c$. Here, $\dot{f}$ is added just to detect the

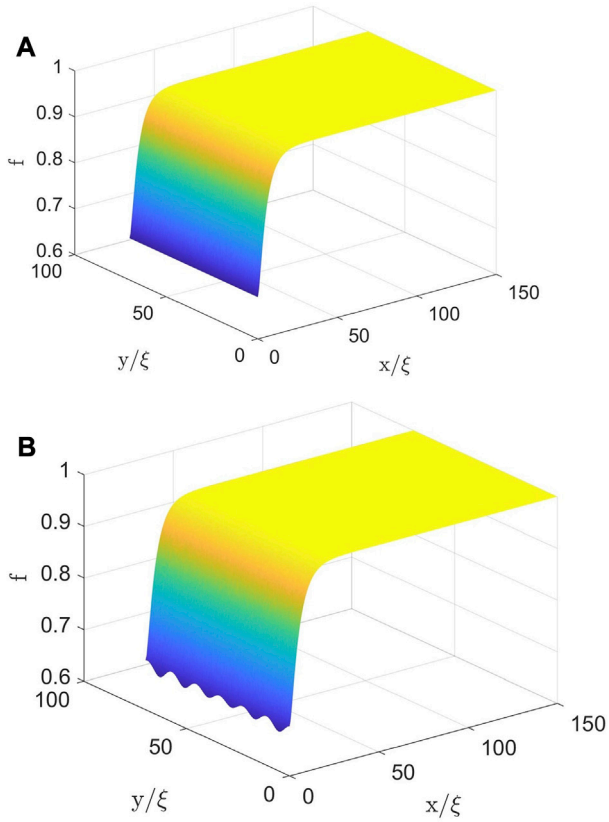

FIGURE 1
Spatial distribution of the order parameter calculated at κ =10, $H_0 = H_{sh} - 0$ **(A)**, and $H_0 = H_{sh} + 0$ **(B)**.

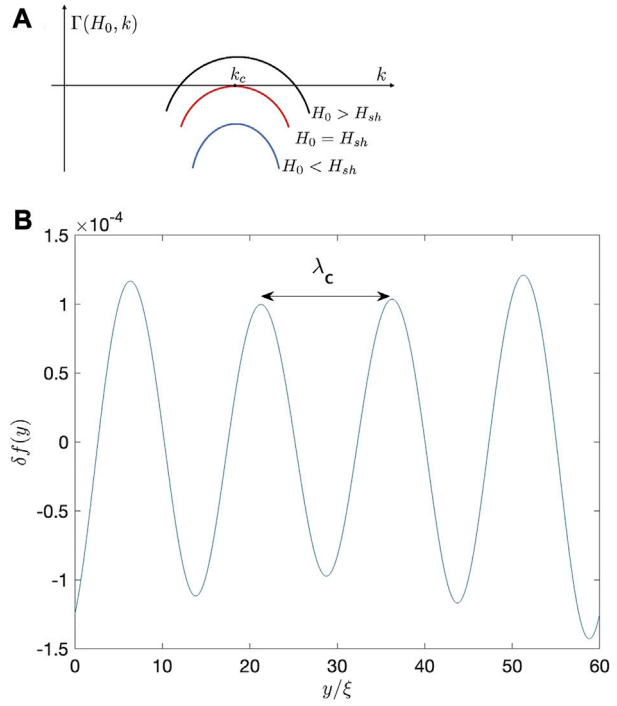

FIGURE 2
(A) Qualitative dependence of the instability increment $\Gamma(H_0, k)$ on the wave vector of perturbation k at different applied fields H_0. **(B)** Snapshot of $\delta f(y)$ at x =0, and $H_0 = H_{sh}$ +0 calculated at κ =10.

instability of the Meissner state in numerical simulations upon slow ramping the applied magnetic field. This procedure allows us to find the field $H_0 = H_{sh}$ above which the GL equations no longer have *stationary* solutions. Another way of numerical calculation of H_{sh} is based on finding the applied field at which the linearized Eqs (1, 2) have zero eigenmode with $\dot{f} = 0$ (Christiansen, 1969; Chapman, 1995; Transtrum et al., 2011; Liarte et al., 2017), as summarized in Supplementary Appendix B. It turns out that the direct solving Eqs (1, 2) with the *ad hoc* term $\dot{f}$ is much faster than solving the eigenmode problem. For slow magnetic ramp rates $\dot{H}_0$ used in our simulations, the resulting H_{sh} calculated by these two methods only differ by ≃ 1%, as it is shown in the next Sections. Equations (1, 2) were solved with the following boundary conditions:

$$\begin{aligned} h(0, y) &= h_0(t), \\ h(x, 0) &= h(x, L_y), \quad f(x, 0) = f(x, L_y), \\ f(L_x, y) &= 1, \quad h(L_x, y) = 0, \end{aligned} \tag{3}$$

where $h_0 = H_0/\sqrt{2}H_c$ and the lengths L_x and L_y of the simulation box $L_x \times L_y$ were chosen to be ≃ (50–150)ξ depending on κ. The details of the numerical calculations are given in the Supplementary Method.

Shown in Figures 1A,B are $f(x, y)$ calculated at κ = 10 and the applied fields H_0 slightly below and above H_{sh}. At $H_0 < H_{sh}$, the order parameter $f(x)$ is reduced at the surface by the flowing screening currents. At $H_0 > H_{sh}$, the stationary $f(x)$ becomes unstable with respect to spontaneously growing periodic perturbations $\delta f(x, y, t)$ along the surface, as shown in Figure 1B. This Turing instability (Cross and Hohenberg, 1993) occurs with respect to a small disturbance $\delta f(x, y, t) \propto \delta f(x) e^{iky+\Gamma t}$, where the increment $\Gamma(H_0, k)$ depends on the wave vector k of spatial oscillations of $f(x, y)$ along the surface as shown in Figure 2A. Below the superheating field, $\Gamma(k)$ is negative so perturbations with all k decay exponentially and the Meissner state is stable. At the superheating field, $\Gamma(k)$ first vanishes at a critical wave number $k = k_c$ at which $\Gamma(k)$ is maximum. At $H_0 = H_{sh} + 0$, the increment $\Gamma(k)$ becomes positive at $k = k_c$, making the Meissner state unstable with respect to a growing critical perturbation $\delta f(x, y, t) \propto \delta f(x) e^{ik_c y + \Gamma(k_c)t}$ with the wavelength $\lambda_c = 2\pi/k_c$, while all other perturbations with $k \neq k_c$ decay exponentially. We calculated H_{sh} by slowly ramping the applied field and detecting the onset of the exponential growth of $f(x, y, t)$ with time as described in Method. The critical wavelength λ_c was evaluated from the maximum peak in the spatial Fourier transform of $\delta f(0, y)$, as shown in Figure 2B. This instability is a precursor of the penetration of the vortex structure with the initial period $\lambda_c \sim (\xi^3\lambda)^{1/4}$ smaller than the stationary vortex spacing $\sim \sqrt{\lambda\xi}$ at $H_0 \simeq H_{sh}$ and $\kappa > 1$. The aforementioned direct method for the calculation of H_{sh} is based on the numerical detection of the field threshold above which the stationary Meissner state does not exist. Here, the time scales of the transition to the vortex state at $H_0 > H_{sh}$ are irrelevant, provided that H_{sh} is calculated at low enough magnetic ramp rates at which H_{sh} is independent of $\dot{h}_0$. We calculated H_{sh} at $\dot{h}_0 \simeq 10^{-5}$ and verified that H_{sh} is indeed practically independent of $\dot{h}_0$, which is also consistent with the calculations of H_{sh} using both the TDGL and full non-equilibrium equations for dirty superconductors (Sheikhzada and Gurevich, 2020).

We then compare some of our numerical results with the known analytical approximations for H_{sh} and k_c at $\kappa \gg 1$, given as follows (Christiansen, 1969; Chapman, 1995; Transtrum et al., 2011; Liarte et al., 2017).

$$\frac{H_{sh}}{H_c} \approx \frac{\sqrt{5}}{3} + \frac{0.545}{\sqrt{\kappa}}, \tag{4}$$

$$\lambda k_c \approx 0.956\kappa^{3/4}. \tag{5}$$

At κ = 10–20, Eqs (4, 5) give the instability wavelength $\lambda_c = 6.57(\xi^3\lambda)^{1/4} \simeq (1.17 - 0.21)\lambda$ and H_{sh} approximately (23–16)% higher than $H_{sh} = 0.745H_c$ in the limit of $\kappa \to \infty$ in which $\lambda_c \to 0$ and the breakdown of the Meissner state at $H = H_{sh}$ occurs once the current density at the surface reaches the depairing limit (Christiansen, 1969). Thus, even at κ = 10–20, characteristic of a dirty Nb or a clean stoichiometric Nb_3Sn (Orlando et al., 1979; Posen and Hall, 2017), the periodic instability along the surface occurs on the scale of the order of the field penetration depth, so the self-consistent GL calculation of H_{sh} is required.

3 Superconductor with an impurity diffusion layer

We consider a dirty layer at the surface with a higher impurity concentration, as shown in Figure 3A. In our simulations, such a layer was modeled by a spatially varying coherence length and penetration depths $\xi^2(x)/\xi_\infty^2 = \lambda_\infty^2/\lambda^2(x) = 1 - \alpha\exp(-x/l_d)$, as shown in Figure 3B. Here, ξ_∞ and λ_∞ are the corresponding

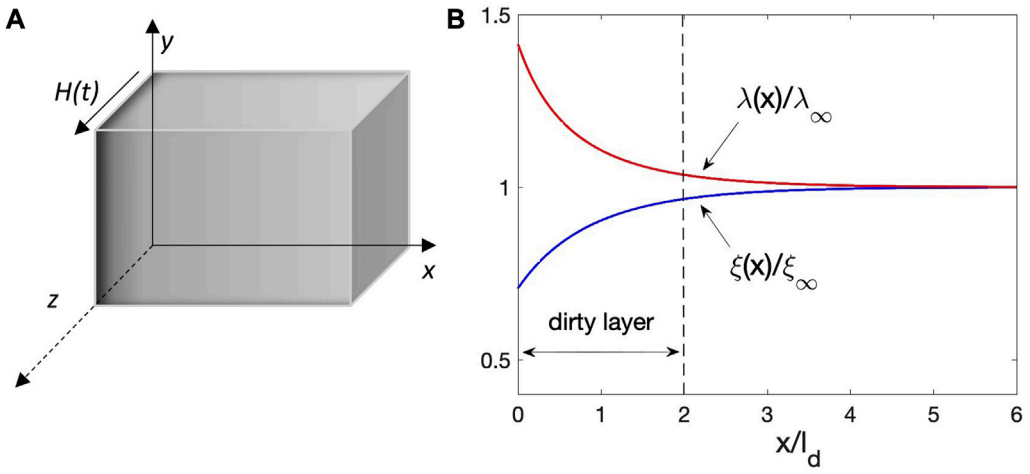

FIGURE 3
(A) Impurity diffusion layer at the surface shown by the dark gray contrast. **(B)** Variations of normalized coherence length and penetration depth across a dirty layer with α =0.5.

bulk values far away from the surface, l_d is the thickness of the diffusion layer, and the parameter $\alpha < 1$ quantifies the reduction of $\xi(0) = (1-\alpha)^{1/2}\xi_\infty$ and the enhancement of $\lambda(0) = (1-\alpha)^{-1/2}\lambda_\infty$ at the surface. The ratio $\xi^2(x)/\xi_\infty^2 = \lambda_\infty^2/\lambda^2(x)$ is controlled by the impurity function $\chi(\hbar v_F/2\pi T_c l(x))$ (Werthamer, 1969) with an inhomogeneous mean free path $l(x)$, which is defined in Supplementary Appendix A. The resulting GL equations take the following form:

$$\dot{f} = f - f^3 + \nabla\cdot\left(S_\gamma \nabla f\right) - \frac{\kappa^2}{S_\gamma f^3}\left[\left(\partial_x h\right)^2 + \left(\partial_y h\right)^2\right], \quad (6)$$

$$\nabla\cdot\left(\frac{\nabla h}{S_\gamma f^2}\right) - \frac{h}{\kappa^2} = 0, \quad (7)$$

where $\kappa = \lambda_\infty/\xi_\infty$, $S_\gamma = \xi^2(x)/\xi_\infty^2 = 1 - \alpha\exp(-x/l_d)$, and the lengths are in units of ξ_∞. The boundary conditions are the same as in Eq. (3). Different impurity profiles were investigated by changing α and l_d at $\kappa = 2$ and $\kappa = 10$, respectively, representing a cleaner and dirtier Nb.

The calculated dependencies of $H_{sh}(l_d)$ on the diffusion layer thickness at different α for $\kappa = 2$ and $\kappa = 10$ are shown in Figures 4A, B, respectively. One can see that $H_{sh}(l_d)$ first increases with l_d, reaches a maximum, and then decreases with l_d approaching a lower value of H_{sh} at $l_d \gg \xi_\infty$. At $\kappa = 2$, $H_{sh}(l_d)$ is maximum at $l_d/\xi_\infty = 0.8, 0.9, 1.5$ for $\alpha = 0.2, 0.5, 0.8$. Similarly, at $\kappa = 10$, $H_{sh}(l_d)$ is maximum at $l_d/\xi_\infty = 4, 5, 10$. Here, the diffusion layer can increase H_{sh} by $\approx 9\%$ at $\kappa = 2$ and by $\approx 14\%$ at $\kappa = 10$ as compared to a superconductor with an ideal surface. A qualitatively similar non-monotonic dependence of H_{sh} on l_d was also obtained by solving the quasiclassical Eilenberger equations in the entire temperature range $0 < T < T_c$ (Ngampruetikorn and Sauls, 2019). The maximum in $H_{sh}(d)$ results from a current counterflow induced in the dirty surface layer by a cleaner substrate with a smaller $\lambda_\infty < \lambda(0)$ (Kubo et al., 2014; Gurevich, 2015), the magnitude of the peak increases as the diffusion layer gets dirtier. The curves $H_{sh}(l_d)$ cross over at larger l_d for which $H_{sh}(\infty)$ is determined by the surface GL parameter $\kappa(0) = \kappa_\infty/(1-\alpha)$. As a result, $H_{sh}(\infty)$ decreases as the material gets dirtier, in agreement with Eq. (4).

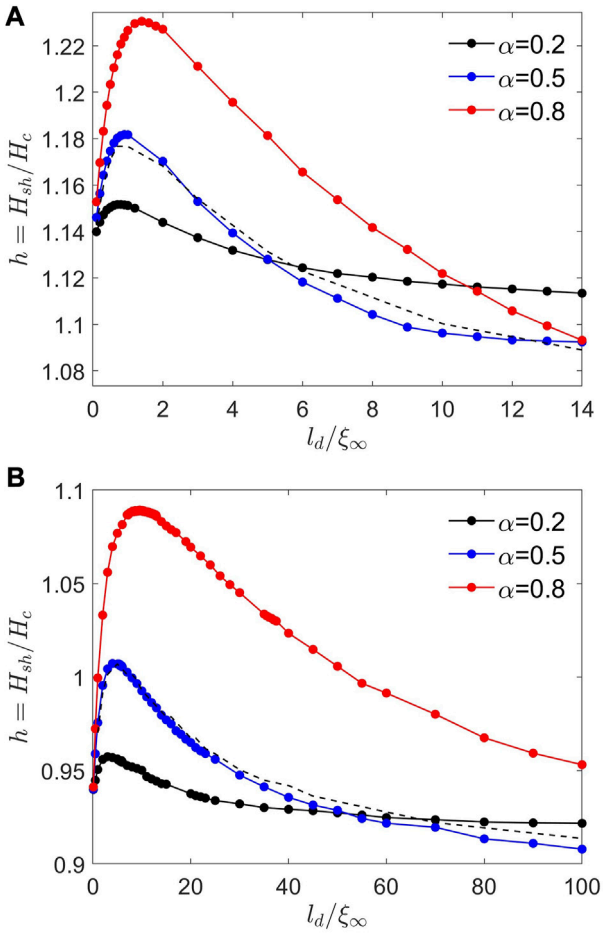

FIGURE 4
Superheating field $H_{sh}(l_d)$ as a function of the dirty layer thickness calculated at **(A)** κ =2 **(B)** κ =10 for different α. The dashed line shows $H_{sh}(l_d)$ calculated from the condition $\delta^2 F$ =0 and $\partial_\kappa \delta^2 F$ =0 at **(A)** κ =2 and **(B)** κ =10 at α =0.5.

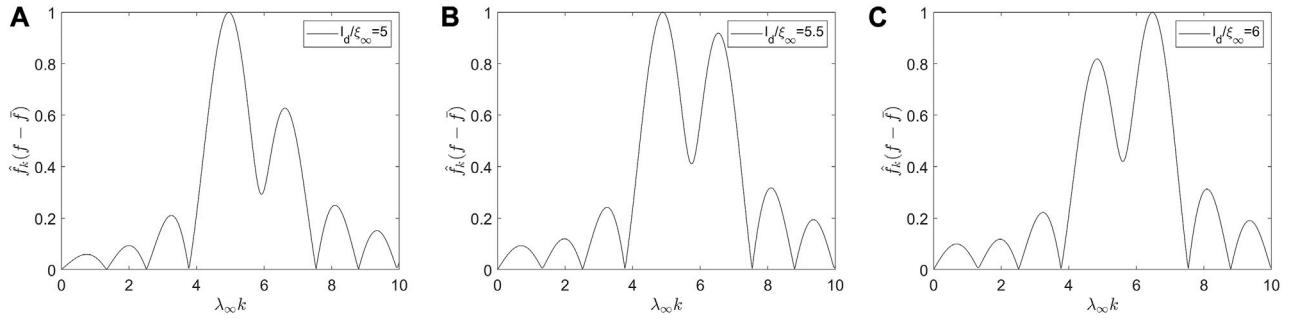

FIGURE 5
Discrete fast Fourier transform of δf (0, y) at $H_0 = H_{sh}$ +0, α =0.5, and κ =10; **(A)** l_d/ξ_∞=5, **(B)** l_d/ξ_∞=5.5, and **(C)** l_d/ξ_∞=6. Evolution of these peaks with l_d/ξ_∞ is shown in "Fourier Transform.gif" in Supplementary Video S1.

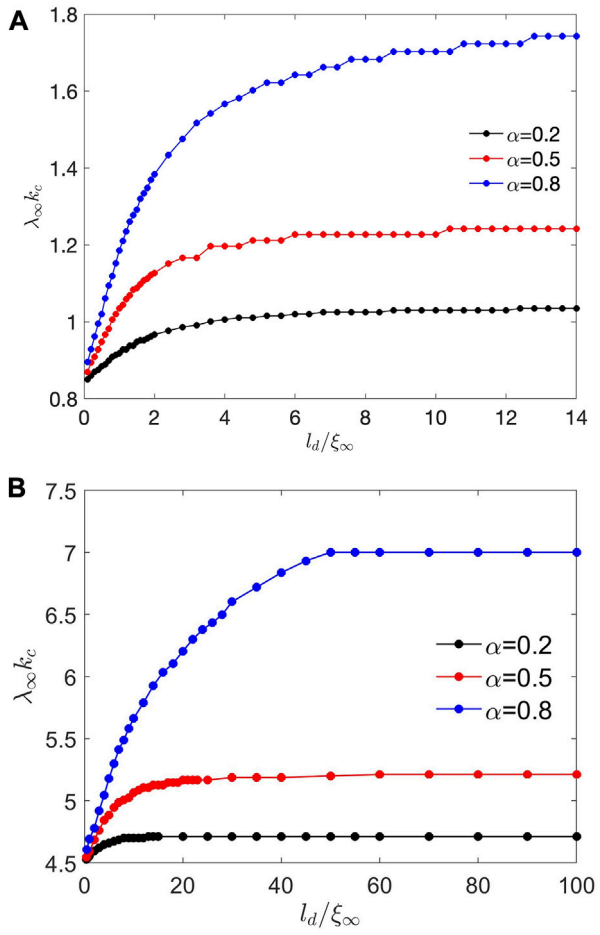

FIGURE 6
Dependencies of λk_c on l_d calculated from the conditions $\delta^2 F$ =0 and $\partial_k \delta^2 F$ =0 at **(A)** κ =2 and **(B)** κ =10 for different α.

The direct numerical calculation of H_{sh} involves detecting the instability of the Meissner state with respect to an infinitesimal perturbation $\delta f(x, y) = \delta f(x) e^{ik_c y + \Gamma t}$ with a finite wave number k_c and an increment $\Gamma(H_0)$ changing the sign from negative at $H_0 < H_{sh}$ to positive at $H_0 > H_{sh}$. Figure 5 shows the fast Fourier transform of a snapshot of $\delta f(0, y, t)$ along y calculated at $H_0 = H_{sh} + 0$ at $\alpha = 0.5$, $\kappa = 10$, and different ratios l_d/ξ_∞. One can see that δf (0, y) has several harmonics even at the slow field ramp rate $\dot{h}_0 = 5 \cdot 10^{-5}$ used in our simulations. Such multi-mode temporal oscillations of δf (0, y) can result from a nonlinear mode coupling above the Turing instability threshold (Cross and Hohenberg, 1993), as well as a finite size of the computational box. In this case, the critical wave number k_c would correspond to the highest peak in the Fourier spectrum of δf_k (0, t). Yet, Figure 5 reveals two uneven peaks whose heights change differently as the ratio l_d/ξ_∞ is varied. For instance, at $l_d/\xi_\infty = 5$, the critical wave number k_c is determined by the higher left peak observed in Figure 5, but as l_d/ξ_∞ is increased to 6, the right peak becomes higher than the left one, so k_c changes jumpwise at $l_d/\xi_\infty \approx 5.5$. The peak shifts toward higher $\lambda_\infty k$ values, providing a constant k_c in this range of l_d/ξ_∞. The switching of k_c between two values as l_d/ξ_∞ is increased can be seen in "Fourier Transform. mp4" in Supplementary Video S1. To see the extent to which this ambiguity in k_c may affect H_{sh}, we have also calculated k_c and H_{sh} from the sign change of the second variation of the free energy $\delta^2 F$ caused by small perturbations of δf (x, y) and δh (x, y). In this method (Christiansen, 1969; Chapman, 1995; Transtrum et al., 2011), H_{sh} is determined by the conditions $\delta^2 F$ (k_c, H_{sh}) = 0 and $\partial \delta^2 F / \partial k_c = 0$. Figures 6A, B show $\lambda_\infty k_c$ as a function of l_d/ξ_∞ at $\kappa = 2$ and $\kappa = 10$ and different α computed from the second variation $\delta^2 F$, as described in Supplementary Appendix B. One can see that the peaks in k_c shown in Figure 5 are in the range of $\lambda k_c \approx 5$–7 qualitatively matching λk_c (l_d) $\approx$ 5 at α = 0.5, as shown in Figure 6. Yet, the $H_{sh}(l_d/\xi_\infty)$ curves calculated by these two methods at α = 0.5 turned out to be very similar (the difference is approximately 1%), as shown by the dashed lines in Figure 4.

4 S-I-S structures

Using the direct simulation method outlined in Section 2, we have calculated $H_{sh}(d)$ and the critical wave number $k_c(d)$ for various S-I-S structures: the S layer of thickness d is separated by an insulator from the S substrate of the same material, a dirty S layer on the top of a cleaner superconductor (e.g., dirty Nb-I-clean Nb), and a thin high T_c overlayer on the top of a low T_c superconductor (e.g., Nb_3Sn-I-Nb). Here, the I layer is assumed to be thick enough to fully suppress

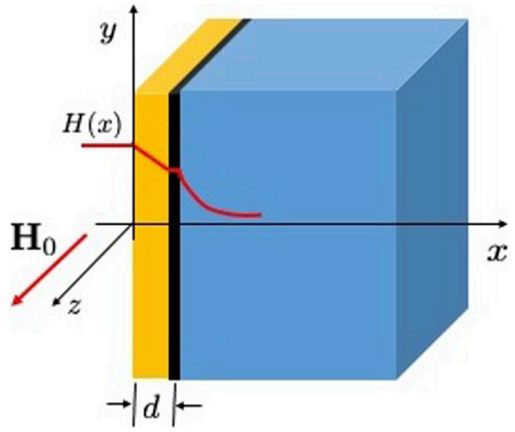

FIGURE 7
Superconductor–insulator–superconductor structure. The vertical black line represents the insulating layer, and the red line shows the screened magnetic field profile $H(x)$.

the Josephson coupling between the S overlayer and the bulk, but thinner than the S overlayer. The screening of the applied field in an S-I-S multilayer is shown in Figure 7.

4.1 S overlayer on the top of the S-substrate

The GL Eqs (1, 2) for the S overlayer separated by the I layer from the substrate made of the same superconductor were solved in both S-domains with the boundary conditions given by Eq. (3) supplemented by the conditions of continuity of $h\ (d + 0,\ y) = h\ (d - 0,\ y)$, parallel electric field $E_y\ (d + 0,\ y) = E_y\ (d - 0,\ y)$, and zero current $\partial_y h\ (d + 0) = \partial_y h\ (d - 0) = 0$ through the I layer. Figure 8 shows that H_{sh} is a function of the thickness of the S overlayer d calculated at $\kappa = 17$ representing Nb_3Sn. Here, a very thin S overlayer reduces $H_{sh}(d)$, which then gradually increases with d, reaching a higher bulk value of H_{sh} at $d > 9\xi_2$, where ξ_2 is the coherence length in the S-substrate. The reduction of $H_{sh}(d)$ at small d results from the I layer blocking the perpendicular currents produced by the critical perturbation and reducing its decay length in the bulk from $\sim \sqrt{\lambda\xi}$ to d. In turn, the critical wave number $k_c(d)$ along the surface shown in Figure 9 increases jumpwise from $k_c \approx 1.8/\lambda_2$ at $d < 9\xi_2$ in a thin overlayer to $k_c \approx 7.2/\lambda_2$ at $d > 9\xi_2$, corresponding to the instability of the Meissner state in a semi-infinite superconductor. The calculated k_c at $d > 9\xi_2$ is approximately 10% smaller than $k_c \approx 8/\lambda_2$ given by the asymptotic Eq. (5) at $\kappa_2 = 17$.

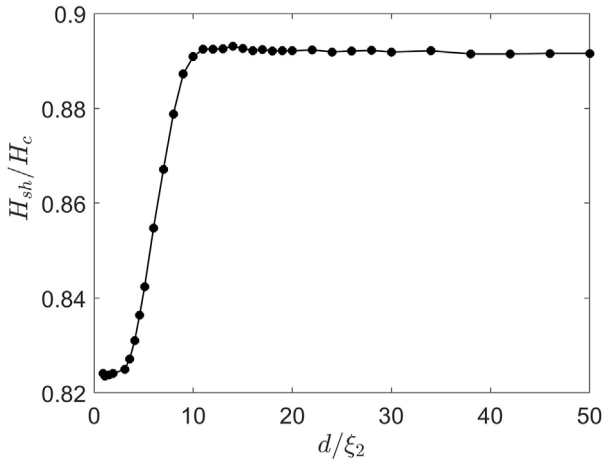

FIGURE 8
Superheating field $H_{sh}(d)$ calculated for the Nb_3Sn-I-Nb_3Sn structure.

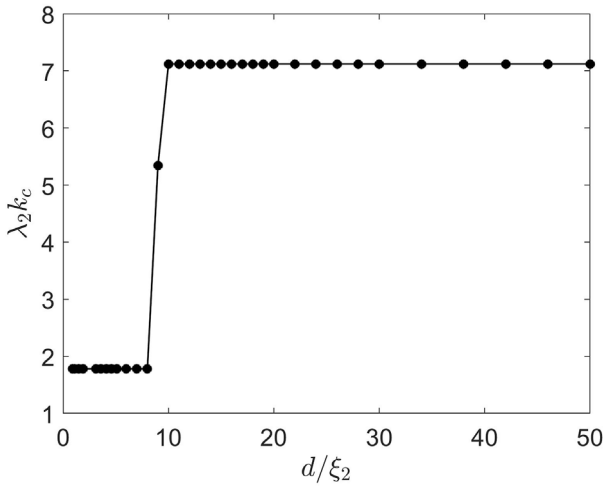

FIGURE 9
Critical wave number $k_c(d)$ calculated for the Nb_3Sn-I-Nb_3Sn structure by solving the quasistatic GL equations directly as described in Section 2.

4.2 Dirty S overlayer on a cleaner S-substrate

A dirty S overlayer with a higher concentration of non-magnetic impurities on a cleaner S substrate of the same material is considered, assuming that both have the same T_c unaffected by non-magnetic impurity scattering (Tinkham, 2004). Superconductivity in the bulk is described by the following GL equations

$$\dot{f}_2 = \nabla^2 f_2 + f_2 - f_2^3 - \frac{\kappa_2^2}{f_2^3}\left[(\partial_x h_2)^2 + \left(\partial_y h_2\right)^2\right], \tag{8}$$

$$\nabla \cdot \left(\frac{\nabla h_2}{f_2^2}\right) = \frac{h_2}{\kappa_2^2}, \tag{9}$$

where index 2 corresponds to the substrate parameters in which the lengths and f_2 are in units of their respective bulk values of ξ_2 and Δ_2. In turn, the GL equations in the overlayer are as follows:

$$\dot{f}_1 = f_1 - f_1^3 + \frac{\xi_1^2}{\xi_2^2}\nabla^2 f_1 - \frac{\xi_1^2}{\xi_2^2}\frac{\kappa_1^2}{f_1^3}\left[(\partial_x h_1)^2 + \left(\partial_y h_1\right)^2\right], \tag{10}$$

$$\nabla \cdot \left(\frac{\nabla h_1}{f_1^2}\right) = \frac{h_1 \xi_2^2}{\xi_1^2 \kappa_1^2}. \tag{11}$$

Equations (8–11) were solved for a dirty Nb_3Sn overlayer on a cleaner Nb_3Sn with a mean free path $l = 2$ nm, $\lambda_1 \approx \lambda_2 (\xi_2/l)^{1/2} \approx 135$

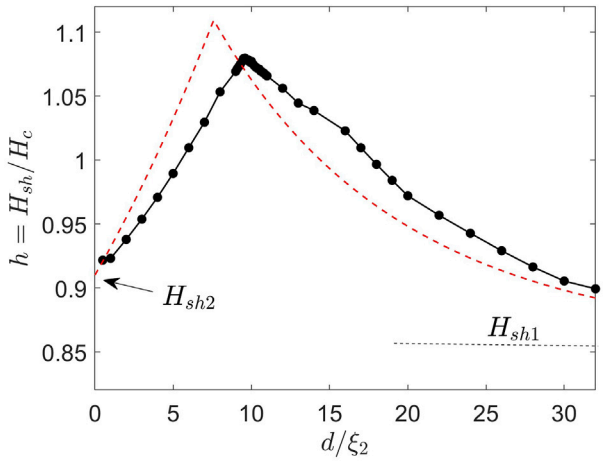

FIGURE 10
Superheating field $H_{sh}(d)$ calculated for the Nb_3Sn(dirty)-I-Nb_3Sn structure. The red dashed line shows $H_{sh}(d)$ calculated from the London Eqs (15–17) with H_{sh1}=0.855H_c and H_{sh2}=0.91H_c taken from the asymptotic limits of $H_{sh}(d)$ at $d \gg \lambda_1$ and d =0, respectively.

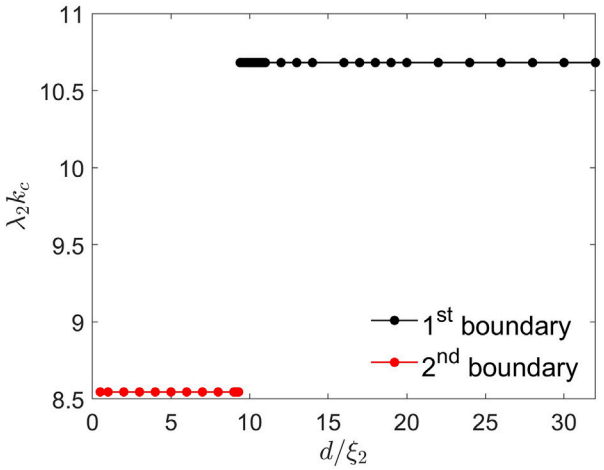

FIGURE 11
The critical wave number $k_c(d)$ calculated for the Nb_3Sn(dirty)-I-Nb_3Sn structure by solving the quasi-static GL equations directly as described in Section 2.

nm, $\xi_1 \approx (l\xi_2)^{1/2} \approx 3$ nm, $\kappa_1 = 45$ in the overlayer, and $\kappa_2 = 17$ in the bulk. Figure 10 shows the calculated dependence of H_{sh} on the overlayer thickness which has a maximum at the optimum thickness $d_m \approx 9\xi_2$. Such an optimal dirty overlayer can increase H_{sh} by approximately 10% as compared to the bulk H_{sh}. The behavior of $H_{sh}(d)$ at a finite κ turns out to be similar to that calculated using the London and GL theories in the limit of $\kappa \to \infty$ in which the enhancement of H_{sh} at $d \simeq d_m$ results from the current counterflow induced by the substrate with a shorter λ_2 in the overlayer with a larger λ_1 (Kubo et al., 2014; Gurevich, 2015). Here, the cusp-like dependence of $H_{sh}(d)$ is controlled by the instability of the Meissner state in the substrate at $d < d_m$ and by the instability of the Meissner state in the overlayer at $d > d_m$, the overlayer partly screening the substrate and allowing it to withstand external fields higher than the bulk H_{sh}. The corresponding critical wave number $k_c(d)$ is shown in Figure 11. The jumpwise change of $k_c(d)$ reflects the switch from the instability of the Meissner state at the inner surface of the substrate at $d < d_m$ to the instability at the outer surface in the overlayer at $d > d_m$. Such a jump in k_c also follows Eq. (5) which gives $k_c\lambda_2 = 0.956\kappa_2^{3/2} \approx 8$ at $d < d_m$ and $k_c\lambda_2 = 0.956\kappa_1^{1/4}\kappa_2^{1/2} \approx 10.2$.

4.3 High-T_c superconducting overlayer

Finally, we consider an S-I-S structure comprising a high-T_c layer on the top of a lower-T_c substrate. The order parameter f_2 and the field h_2 in the substrate are described in Eqs (8, 9), and the GL equations for f_1 and h_1 in the overlayer are given by

$$\dot{f}_1 = \zeta f_1 - f_1^3 + s\nabla^2 f_1 - \frac{\tilde{\kappa}^2}{f_1^3}\left[(\partial_x h_1)^2 + (\partial_y h_1)^2\right], \tag{12}$$

$$\nabla \cdot \left(\frac{\nabla h_1}{f_1^2}\right) = \frac{\lambda_2^2 h_1}{\lambda_1^2 \zeta \kappa_2^2}, \tag{13}$$

$$\zeta = \frac{1 - T/T_{c1}}{1 - T/T_{c2}}, \qquad s = \frac{\xi_1^2}{\xi_2^2}\zeta, \qquad \tilde{\kappa}^2 = \frac{\xi_1^2\lambda_1^4}{\xi_2^2\lambda_2^4}\kappa_2^2\zeta^3, \tag{14}$$

where T_{c1} and T_{c2} are the critical temperatures of the overlayer and the substrate, respectively, and the order parameter and lengths are normalized to the respective parameters of the substrate. Equations (12–14) are supplemented by the boundary conditions given by Eq. (3) and the conditions of field continuity and zero current through the I layer.

We solved the GL equations for a clean Nb_3Sn overlayer on a bulk Nb using $\kappa_2 = 50/22$ and $\kappa_1 = 17$ (Orlando et al., 1979; Posen and Hall, 2017). The calculated superheating field $H_{sh}(d)$ shown in Figure 12 has a maximum at $d_m \approx 4\xi_2$. This behavior of $H_{sh}(d)$ is similar to that of $H_{sh}(d)$ considered in the previous section: $H_{sh}(d)$ at $d < d_m$ is limited by the instability of the Meissner state in the Nb substrate partly screened by the Nb_3Sn overlayer, while

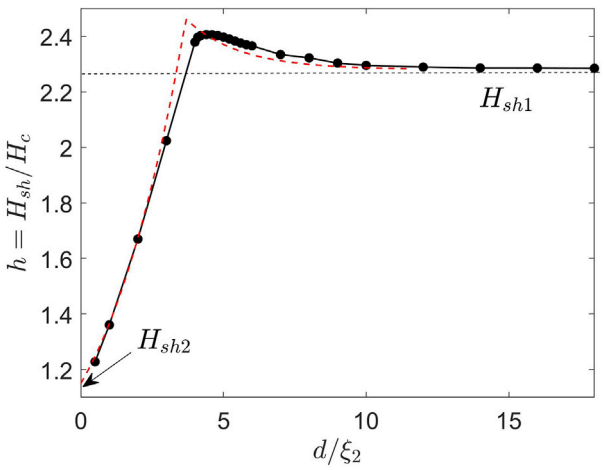

FIGURE 12
Superheating field $H_{sh}(d)$ calculated for the Nb_3Sn-I-Nb structure. The red dashed line shows $H_{sh}(d)$ calculated from the London Eqs (15–17) with H_{sh1}=2.28H_c and H_{sh2}=1.08H_c taken from the asymptotic limits of $H_{sh}(d)$ at $d \gg \lambda_1$ and d =0, respectively.

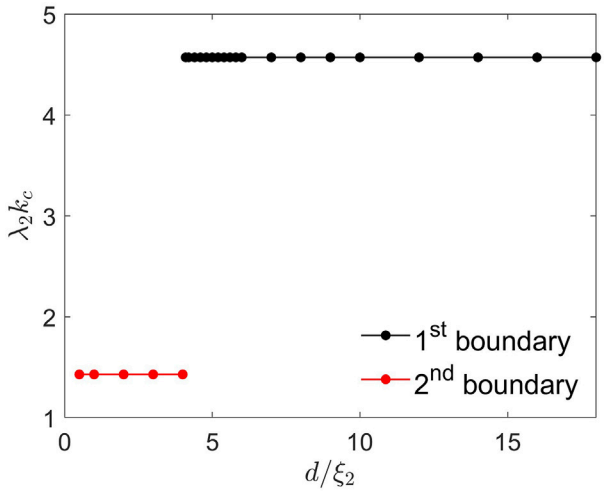

FIGURE 13
The critical wave number $k_c(d)$ calculated for the Nb_3Sn-I-Nb structure by solving the quasistatic GL equations directly as described in Section 2.

H_{sh} at $d > d_m$ is determined by the superheating field of Nb_3Sn enhanced at $d \approx d_m$ by the current counterflow caused by the Nb substrate. The corresponding dependence of $k_c(d)$ on the overlayer thickness is shown in Figure 13. The jumpwise change of $k_c(d)$ reflects the switch from the instability of the Meissner state at the inner surface of the low-T_c substrate at $d < d_m$ to the instability at the outer surface in the high-T_c overlayer at $d > d_m$, which is similar to that shown in Figure 11. For the parameters used in the simulations, such Nb_3Sn-I-Nb structures with $d \approx d_m$ can boost the superheating field up to ~ 2.2 times higher than the bulk H_{sh2} of Nb (Gurevich, 2006; Gurevich, 2015) and approximately 5.3% higher than the bulk H_{sh1} of Nb_3Sn.

5 Discussion

The GL calculations of the DC superheating field at $T \approx T_c$ self-consistently take into account the essential non-linear field screening and the periodic instability of the Meissner state in the entire range of the GL parameters which can be tuned by the impurities. This approach shows that the thicknesses of the impurity diffusion layer or S-I-S layers can be optimized to increase H_{sh} above the superheating fields of individual components. For instance, optimizing the diffusion length can enhance H_{sh} by ≃ 5–20% at $\kappa = 10$ and by ≃ 2–9% at $\kappa = 2$. An optimized dirty Nb_3Sn overlayer deposited onto the Nb_3Sn field by ≃ 10% as compared to H_{sh} of a clean Nb_3Sn. This effect manifests itself in a non-monotonic dependence of H_{sh} on the dirty layer thickness due to the current counterflow induced at the surface by a superconducting substrate with a shorter field penetration depth. Such behavior of $H_{sh}(d)$ is consistent with the previous calculations of H_{sh} based on the London (Gurevich, 2006; Gurevich, 2015; Kubo et al., 2014) or Usadel (Kubo, 2021) and Eilenberger (Ngampruetikorn and Sauls, 2019) theories at $\kappa \to \infty$. To see the extent to which the London model is consistent with the GL results, we consider $H_{sh}(d)$ calculated for an S-I-S multilayer in the London limit (Gurevich, 2015).

$$H_{sh}(d) = [\cosh(d/\lambda_1) + (\lambda_2/\lambda_1)\sinh(d/\lambda_1)]H_{sh2}, \quad d < d_m \tag{15}$$

$$H_{sh}(d) = \left[\frac{\lambda_1 + \lambda_2 \tanh(d/\lambda_1)}{\lambda_1 \tanh(d/\lambda_1) + \lambda_2}\right]H_{sh1}, \quad d > d_m \tag{16}$$

$$d_m = \lambda_1 \ln\left\{\frac{\lambda_1}{\lambda_1 + \lambda_2}\left[\frac{H_{sh1}}{H_{sh2}} + \sqrt{\frac{H_{sh1}^2}{H_{sh2}^2} + 1 - \frac{\lambda_2^2}{\lambda_1^2}}\right]\right\}, \tag{17}$$

where H_{sh1} and H_{sh2} are the bulk superheating fields of the overlayer and the substrate, respectively. Equation (15) describes $H_{sh}(d)$ of S-I-S structures with thin overlayers ($d < d_m$), where the Meissner state first breaks down at the surface of the substrate. Here, the high-H_c overlayer partly screens the substrate, allowing it to stay in the Meissner state at a higher applied field $H_0 = H_{sh}(d)$ than the bare substrate. If $d > d_m$, the Meissner state first breaks down at the outer surface of the overlayer so that $H_{sh}(d) \to H_{sh1}$ at $d \gg \lambda_1$. The maximum $H_{sh}(d_m)$ is given by:

$$H_{sh}(d_m) = \left[H_{sh1}^2 + \left(1 - \frac{\lambda_2^2}{\lambda_1^2}\right)H_{sh2}^2\right]^{1/2}. \tag{18}$$

The maximum $H_{sh}(d_m) = (H_{sh1}^2 + H_{sh2}^2)^{1/2}$ in an S-I-S multilayer occurs if $(\lambda_2/\lambda_1)^2 \ll 1$.

Equations (15–17) do not take into account the reduction of the superfluid density by current, non-linear field screening and the periodic instability of the Meissner state at a finite κ. The London model does not account for the size effect of reducing $H_{sh}(d)$ if the overlayer thickness is smaller than the decay length ~ $\sqrt{\lambda_1 \xi_1}$ of the critical perturbation, as was discussed in Section 4.1. Indeed, for identical materials of the substrate and overlayer ($\lambda_1 = \lambda_2$, $H_{sh1} = H_{sh2}$), Eqs (15–17) give $d_m = 0$ and $H_{sh}(d) = H_{sh1}$ independent of d, which is inconsistent with the reduction of $H_{sh}(d)$ at $d \lesssim 10\xi_2$, as shown in Figure 8. Yet, the London model captures the non-monotonic thickness dependence $H_{sh}(d)$ calculated from the GL theory if the overlayer has different properties than those of the substrate, and the input parameters H_{sh1} and H_{sh2} in Eqs (15–17) are exact bulk superheating fields for given values of κ and H_c, respectively (Gurevich, 2015). For instance, Figure 10 compares the GL and the London $H_{sh}(d)$ calculated for an Nb_3Sn(dirty)-I-Nb_3Sn structure with a dirty overlayer for which the London model works reasonably well. For the Nb_3Sn-I-Nb multilayers considered in Section 4.3, we observed a rather good agreement between $H_{sh}(d)$ calculated from the GL theory and Eqs (15–17), as shown in Figure 12. Such surprising accuracy of Eqs (15–17) was also observed by Kubo (2021) in the Usadel simulations of dirty S-I-S multilayers in the entire temperature range of $0 < T < T_c$ at $\kappa \to \infty$.

In the GL region $T \approx T_{c2}$, Eqs (15–17) predict a significant change in the temperature dependence of $H_{sh}(T)$ of the S-I-S multilayer with a higher-T_c overlayer as compared to $H_{sh2}(T)$ of the bare substrate. If $T \to T_{c2}$, the penetration depth $\lambda_2(T) \propto (T_{c2} - T)^{-1/2}$ diverges and $H_{sh2}(T) \propto T_{c2} - T$ vanishes, while λ_1 and H_{sh1} remain nearly independent of T. This case is characteristic of Nb_3Sn-I-Nb for which $T_{c1} \simeq 2T_{c2}$, the crossover thickness $d_m(T)$ increases with T and diverges logarithmically at $T \to T_{c2}$. In turn, $H_{sh}(d, T)$ obtained by Eq. (15) is limited by the small superheating field of the substrate partially screened by the high-T_c overlayer:

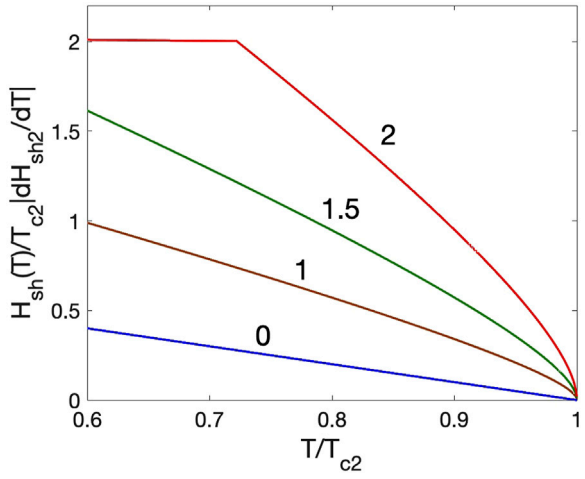

FIGURE 14
Temperature dependencies of $H_{sh}(T)$ calculated from Eqs (15–17) for different ratios d/λ_1 and the superconducting parameters of Nb_3Sn-I-Nb specified in the text. The sharp change in the behavior of $H_{sh}(T)$ upon decreasing T at d/λ_1=2 occurs as $d_m(T)$ becomes shorter than d and $H_{sh}(T)$ crosses over to a nearly constant $H_{sh1}(T)$ of the overlayer. For smaller d/λ_1, such a transition in $H_{sh}(T)$ takes place at lower T outside the GL temperature range shown in the figure. Here, the blue line with d/λ_1=0 represents $H_{sh2}(T)$ of the bare substrate.

$$H_{sh}(T) \simeq (\lambda_2/\lambda_1)\sinh(d/\lambda_1)H_{sh2}(T) \propto \sqrt{T_{c2}-T}, \qquad (19)$$

Hence, $H_{sh}(T)$ can be significantly higher than $H_{sh2}(T) \propto T_{c2} - T$ at $T \approx T_{c2}$, particularly if $d > \lambda_1$. As an illustration, Figure 14 shows $H_{sh}(T)$ calculated from Eqs (15–17) for different ratios d/λ_1 and the parameters of Nb_3Sn-I-Nb specified in Section 4.3. One can see both the square root temperature dependence given by Eq. (19) at $T \approx T_{c2}$ and a sharp change in $H_{sh}(T)$ upon decreasing T as $d_m(T)$ becomes shorter than d and $H_{sh}(T)$ crosses over to a nearly constant $H_{sh1}(T)$ of the overlayer. For $d/\lambda_1 < 2$, such a transition in $H_{sh}(T)$ happens at lower T outside the GL temperature range shown in the figure.

The relation between the static H_{sh} calculated here and the dynamic superheating field $H_{sd}(T, \omega)$ representing the fundamental field limit of superconductivity breakdown in SRF cavities depends on the rf frequency ω, temperature, and the material purity (Gurevich, 2023). The calculation of H_{sd} for S-I-S structures generally requires solving complex equations of non-equilibrium superconductivity, which in some cases can be reduced to TDGL equations at $T \approx T_c$ (Watts-Tobin et al., 1981). The dynamic superheating field of an alloyed superconductor with an ideal surface at $T \approx T_c$ was calculated from the microscopic theory (Sheikhzada and Gurevich, 2020), where it was shown that $H_{sd}(T)$ approaches the static $H_{sh}(T)$ at low frequencies $\omega \ll \omega_c$ but can be by a factor $\sqrt{2}$ larger than H_{sh} at $\omega \gg \omega_c$. Here, the crossover frequency $\omega_c \sim \min(\tau_\epsilon^{-1}, \tau_\Delta^{-1})$ is set by the inelastic electron–phonon scattering time $\tau_\epsilon(T) \propto T^{-3}$ and the TDGL relaxation time of the order parameter $\tau_\Delta = \pi\hbar/8k_B(T_c - T)$ (Gurevich, 2023). For Nb and Nb_3Sn at $T \approx T_c^{Nb} = 9.2$ K, both $\tau_\epsilon(9K) \sim 10^{-11}$ s and $\tau_\Delta \sim 10^{-11}$ s at $T_c - T = 0.2$ K are much shorter than the rf period at 1 GHz. In this case, the superconducting and quasiparticle screening currents follow practically instantaneously the driving rf field, and the quasistatic $H_{sh}(T)$ considered here is applicable. The dynamic superheating field at lower temperatures $T \simeq 2$ K at GHz frequencies has not yet been calculated from a microscopic theory.

In this work, H_{sh} was calculated for S-I-S structures with ideal surfaces and interfaces without topographical and material defects or weakly coupled grain boundaries in the overlayer and the substrate. Topographical and other surface defects can locally reduce the field onset of the dissipative penetration of vortices and reduce the global H_{sh}, as was shown by TDGL simulations (Vodolazov, 2000; Pack et al., 2020; Wang et al., 2022). Likewise, $H_{sh}(T)$ can be reduced by weakly coupled grain boundaries causing premature proliferation of mixed Abrikosov–Josephson vortices or phase slips (Sheikhzada and Gurevich, 2017). The I interlayer in S-I-S coating can mitigate these detrimental effects by the following: 1. increasing the cavity breakdown field by thin high-H_c overlayers and 2. confining vortices penetrating at surface defects in a thin overlayer and blocking flux penetration in the cavity wall, where it can trigger thermo-magnetic avalanches, causing global superconductivity breakdown (Gurevich, 2015; Gurevich, 2023). The S-I-S coating can provide these two goals if the overlayer thickness does not exceed λ_1 (Gurevich, 2006). In this work, we calculated the upper limit of H_{sh} and showed how the S-I-S geometry can be optimized to increase H_{sh} at $d \lesssim \lambda_1$.

6 Conclusion

Our numerical GL calculations of the DC superheating field in superconductors with nanostructured surfaces cover the entire range of $1 < \kappa < \infty$ and account for both the non-linear Meissner screening and the instability with a finite wave number k_c at $H_0 = H_{sh}$. We showed that there are optimum thicknesses of the impurity diffusion layer and the superconducting overlayer which maximize H_{sh}. These results suggest the possible ways of increasing the breakdown fields by surface nanostructuring and can help understand the ways of optimizing SRF cavities to achieve higher accelerating gradients.

Data availability statement

The original contributions presented in the study are included in the article/Supplementary Material; further inquiries can be directed to the corresponding author.

Author contributions

WP performed all numerical simulations, analyzed the results, and wrote the first draft of the manuscript. AG initiated and supervised the project and wrote the revised manuscript. All authors contributed to the article and approved the submitted version.

Funding

This work was supported by DOE under grant DE-SC 100387–020 (ODU) and by the Virginia Military Institute (VMI).

Conflict of interest

The authors declare that the research was conducted in the absence of any commercial or financial relationships that could be construed as a potential conflict of interest.

Publisher's note

All claims expressed in this article are solely those of the authors and do not necessarily represent those of their affiliated organizations, or those of the publisher, the editors, and the reviewers. Any product that may be evaluated in this article, or claim that may be made by its manufacturer, is not guaranteed or endorsed by the publisher.

Supplementary material

The Supplementary Material for this article can be found online at: https://www.frontiersin.org/articles/10.3389/femat.2023.1246016/full#supplementary-material

References

Catelani, G., and Sethna, J. P. (2008). Temperature dependence of the superheating field for superconductors in the high-κ London limit. *Phys. Rev. B* 78, 224509. doi:10.1103/PhysRevB.78.224509

Chapman, S. J. (1995). Superheating field of type II superconductors. *SIAM J. Appl. Math.* 55 (5), 1233–1258. doi:10.1137/S0036139993254760

Christiansen, P. V. (1969). Magnetic superheating field in high-κ superconductors. *Solid State Commun.* 7 (10), 727–729. doi:10.1016/0038-1098(69)90652-8

Ciovati, G., Myneni, G., Stevie, F., Maheshwari, P., and Griffis, D. (2010). High field Q slope and the baking effect: review of recent experimental results and new data on Nb heat treatments. *Phys. Rev. St. Accel. Beams* 13, 022002. doi:10.1103/PhysRevSTAB.13.022002

Ciovati, G., Dhakal, P., and Myneni, G. (2016). Superconducting radio-frequency cavities made from medium and low-purity niobium ingots. *Supercond. Sci. Technol.* 29, 064002. doi:10.1088/0953-2048/29/6/064002

COMSOL COMSOL Multiphysics modeling software. Available at: https://www.comsol.com (Accessed March 15, 2017).

Cross, M. C., and Hohenberg, P. C. (1993). Pattern formation outside of equilibrium. *Rev. Mod. Phys.* 65, 851–1112. doi:10.1103/RevModPhys.65.851

Dhakal, P. (2020). Nitrogen doping and infusion in SRF cavities: A review. *Open Phys. J.* 5, 100034. doi:10.1016/j.physo.2020.100034

Galaiko, V. P. (1966). Stability limits of the superconducting state in a magnetic field for superconductors of the second kind. *Zh. Exp. Teor. Fiz.* 50, 717–723.

Grassellino, A., Romanenko, A., Trenikhina, Y., Checchin, M., Martinello, M., Melnychuk, P., et al. (2017). Unprecedented quality factors at accelerating gradients up to 45 MVm^{-1} in niobium superconducting resonators via low temperature nitrogen infusion. *Supercond. Sci. Technol.* 30, 094004. doi:10.1088/1361-6668/aa7afe

Gurevich, A. (2006). Enhancement of rf breakdown field of superconductors by multilayer coating. *Appl. Phys. Lett.* 88 (1), 012511. doi:10.1063/1.2162264

Gurevich, A., and Kubo, T. (2017). Surface impedance and optimum surface resistance of a superconductor with an imperfect surface. *Phys. Rev. B* 96, 184515. doi:10.1103/PhysRevB.96.184515

Gurevich, A. (2015). Maximum screening fields of superconducting multilayer structures. *AIP Adv.* 5 (1), 017112. doi:10.1063/1.4905711

Gurevich, A. (2023). Tuning microwave losses in superconducting resonators. *Supercond. Sci. Technol.* 36, 063002. doi:10.1088/1361-6668/acc214

Kubo, T., Iwashita, Y., and Saeki, T. (2014). Radio-frequency electromagnetic field and vortex penetration in multilayered superconductors. *Appl. Phys. Lett.* 104, 032603. doi:10.1063/1.4862892

Kubo, T. (2021). Superheating fields of semi-infinite superconductors and layered superconductors in the diffusive limit: structural optimization based on the microscopic theory. *Supercond. Sci. Technol.* 34, 045006. doi:10.1088/1361-6668/abdedd

Lechner, E. M., Angle, J. W., Stevie, F. A., Kelley, M. J., Reece, C. E., and Palczewski, A. D. (2021). RF surface resistance tuning of superconducting niobium via thermal diffusion of native oxide. *Appl. Phys. Lett.* 119, 082601. doi:10.1063/5.0059464

Liarte, D. B., Posen, S., Transtrum, M. K., Catelani, G., Liepe, M., and Sethna, J. P. (2017). Theoretical estimates of maximum fields in superconducting resonant radio frequency cavities: stability theory, disorder, and laminates. *Supercond. Sci. Technol.* 30, 033002. doi:10.1088/1361-6668/30/3/033002

Lin, F. P. J., and Gurevich, A. (2012). Effect of impurities on the superheating field of type-II superconductors. *Phys. Rev. B* 85 (5), 054513. doi:10.1103/PhysRevB.85.054513

Matricon, J., and Saint-James, D. (1967). Superheating fields in superconductors. *Phys. Lett. A* 24 (5), 241–242. doi:10.1016/0375-9601(67)90412-4

MATLAB Matlab. Available at: https://www.mathworks.com/products/matlab.html (Accessed March 15, 2017).

Ngampruetikorn, V., and Sauls, J. A. (2019). Effect of inhomogeneous surface disorder on the superheating field of superconducting RF cavities. *Phys. Rev. Res.* 1, 012015. doi:10.1103/PhysRevResearch.1.012015

Orlando, T. P., McNiff, E. J., Foner, S., and Beasley, M. R. (1979). Critical fields, Pauli paramagnetic limiting, and material parameters of Nb_3Sn and V_3Si. *Phys. Rev. B* 19, 4545–4561. doi:10.1103/physrevb.19.4545

Pack, A. R., Carlson, J., Wadsworth, S., and Transtrum, M. K. (2020). Vortex nucleation in superconductors within time-dependent Ginzburg-Landau theory in two and three dimensions: role of surface defects and material inhomogeneities. *Phys. Rev. B* 101, 144504. doi:10.1103/PhysRevB.101.144504

Padamsee, H., Knobloch, J., and Hays, T. (2018). *RF superconductivity for accelerators*. 2nd ed. Germany: Wiley-VCH Verlag GmbH and Co. KGaA.

Posen, S., and Hall, D. L. (2017). Nb_3Sn superconducting radiofrequency cavities: fabrication, results, properties, and prospects. *Supercond.* Sci. Technol. 30, 033004. doi:10.1088/1361-6668/30/3/033004

Posen, S., Romanenko, A., Grassellino, A., Melnychuk, O. S., and Sergatskov, D. A. (2020). Ultralow surface resistance via vacuum heat treatment of superconducting radio-frequency cavities. *Phys. Rev. Appl.* 13, 014024. doi:10.1103/PhysRevApplied.13.014024

Sheikhzada, A., and Gurevich, A. (2020). Dynamic pair-breaking current, critical superfluid velocity, and nonlinear electromagnetic response of nonequilibrium superconductors. *Phys. Rev. B* 102, 104507. doi:10.1103/PhysRevB.102.104507

Sheikhzada, A., and Gurevich, A. (2017). Dynamic transition of vortices into phase slips and generation of vortex-antivortex pairs in thin film Josephson junctions under dc and ac currents. *Phys. Rev. B* 95, 214507. doi:10.1103/PhysRevB.95.214507

Tinkham, M. (2004). *Introduction to superconductivity*. New York: Dover Publication.

Transtrum, M. K., Catelani, G., and Sethna, J. P. (2011). Superheating field of superconductors within Ginzburg-Landau theory. *Phys. Rev. B* 83 (9), 094505. doi:10.1103/PhysRevB.83.094505

Vodolazov, D. Yu. (2000). Effect of surface defects on the first field for vortex entry in type-II superconductors. *Phys. Rev. B* 62, 8691–8694. doi:10.1103/PhysRevB.62.8691

Wang, Q-Y., Xue, C., Dong, C. C., and Zhou, Y-H. (2022). Effects of defects and surface roughness on the vortex penetration and vortex dynamics in superconductor–insulator–superconductor multilayer structures exposed to RF magnetic fields: numerical simulations within TDGL theory. *Supercond. Sci. Technol.* 35, 045004. doi:10.1088/1361-6668/ac4ad1

Watts-Tobin, R. J., Krähenbühl, Y., and Kramer, L. (1981). Nonequilibrium theory of dirty, current-carrying superconductors: phase-slip oscillators in narrow filaments near T_c. *J. Low. Temp. Phys.* 42, 459–501. doi:10.1007/BF00117427

Werthamer, N. R. (1969). in *Superconductivity*. Editor R. D. Parks (New York: Marcel Dekker Inc.), 321–370.